

SlowFast-SCI: Slow-Fast Deep Unfolding Learning for Spectral Compressive Imaging

Haijin Zeng^{1,*} Xuan Lu^{2,*} Yurong Zhang³ Qiangqiang Shen⁴ Guoqing Chao⁵
Li Jiang⁶ Yongyong Chen^{2,†}

¹Harvard University ²Harbin Institute of Technology, Shenzhen

³Shanghai Jiaotong University ⁴City University of Hong Kong

⁵Harbin Institute of Technology, Weihai ⁶The Chinese University of Hong Kong, Shenzhen

Abstract

Humans learn in two complementary ways: a slow, cumulative process that builds broad, general knowledge, and a fast, on-the-fly process that captures specific experiences. Existing deep-unfolding methods for spectral compressive imaging (SCI) mirror only the slow component—relying on heavy pre-training with many unfolding stages—yet they lack the rapid adaptation needed to handle new optical configurations. As a result, they falter on out-of-distribution cameras, especially in bespoke spectral setups unseen during training. This depth also incurs heavy computation and slow inference. To bridge this gap, we introduce SlowFast-SCI, a dual-speed framework seamlessly integrated into any deep unfolding network beyond SCI systems. During slow learning, we pre-train or reuse a priors-based backbone and distill it via imaging guidance into a compact fast-unfolding model. In the fast learning stage, lightweight adaptation modules are embedded within each block and fine-tuned self-supervised at test time via a self-supervised loss—without retraining the backbone. To the best of our knowledge, SlowFast-SCI is the first test-time adaptation-driven deep unfolding framework for efficient, self-adaptive spectral reconstruction. Its dual-stage design unites offline robustness with on-the-fly per-sample calibration—yielding over 70% reduction in parameters and FLOPs, up to 5.79 dB PSNR improvement on out-of-distribution data, preserved cross-domain adaptability, and a 4× faster adaptation speed. In addition, its modularity integrates with any deep-unfolding network, paving the way for self-adaptive, field-deployable imaging and expanded computational imaging modalities. The models, datasets, and code are available at <https://github.com/XuanLu11/SlowFast-SCI>.

*Equal contribution. {haijin.zeng2018, xuanlu1113}@gmail.com

†Corresponding author. cyy2020@hit.edu.cn

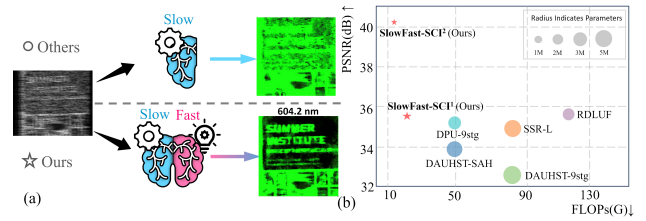


Figure 1. (a) Previous SCI reconstruction method vs. our SlowFast-SCI. (b) The PSNR-FLOPs-Params analysis comparing the proposed SlowFast-SCI with latest state-of-the-art methods.

1. Introduction

Humans are endowed with a complementary learning system [15, 22] that operates on two distinct timescales. A slow process in the neocortex gradually integrates diverse experiences into a coherent world model, enabling robust prediction of action outcomes [32]. In parallel, a fast process in the hippocampus rapidly encodes episodic details, supporting agile adaptation to novel circumstances [34]. Integrating such a dual-speed mechanism into neural networks enables rapid adaptation, *i.e.*, swift recalibration to new domains or unseen inputs—thereby enhancing both flexibility and generalization.

This dual-speed learning paradigm inspires advances in spectral compressive imaging (SCI), a computational photography technique that aims to reconstruct rich hyperspectral information from compressed measurements. The predominant SCI architecture, coded aperture snapshot spectral imaging (CASSI) [13, 24, 36], employs a spatially coded mask and a dispersive element to modulate, shift, and integrate spectral bands onto a two-dimensional sensor [45], achieving high-throughput, cost-effective, and bandwidth-efficient acquisition. The resulting hyperspectral images (HSIs) deliver rich spatial-spectral signatures that significantly enhance scene characterization beyond conventional RGB imagery. Consequently, SCI has found broad applications across computer vision and remote sensing, *e.g.*, object detection [18, 35], medical imaging [21,

25], and land-cover classification [2, 39].

Based on the CASSI acquisition model, a broad spectrum of reconstruction algorithms has been proposed to recover a three-dimensional hyperspectral data cube from its two-dimensional measurement. Traditional model-based methods employ handcrafted priors—such as sparsity [19, 36], total variation [31, 38], and low-rank constraints [20, 44]—but they require careful parameter tuning and often yield suboptimal quality and slow convergence. The advent of deep learning introduced end-to-end networks that significantly improve both reconstruction accuracy and speed [4–7, 12, 16, 23, 24, 42, 43].

In particular, deep unfolding frameworks (DUNs) unroll iterative optimization into trainable layers, thereby integrating model-driven regularization with data-driven learning [6, 12, 17, 23, 42]. However, these methods depend on extensive pre-training over large, paired datasets—an impractical requirement given the scarcity and acquisition cost of real HSI data, reflecting only the slow component of learning. Moreover, to achieve state-of-the-art performance, deep unfolding approaches often employ a large number of sequential unfolding blocks; each block must process the full high-dimensional hyperspectral volume, which greatly increases computational and memory burdens. This level of complexity not only complicates training and inference but also makes such architectures impractical for real-world applications and deployment on resource-constrained devices.

Per-sample adaptation—analogueous to human fast learning—is essential for robust SCI reconstruction under scarce HSI data. While recent advances such as self-supervised fine-tuning and test-time adaptation enable rapid calibration, applying them directly to deep unfolding networks proves problematic: full-network fine-tuning destabilizes sequential stages and linear probes cannot accommodate layer-wise inference. SAH-SCI [41] supports general self-supervised tuning but lacks runtime adaptation, and recent test-time adaptation (TTA) methods [27, 28, 47] have yet to address hyperspectral SCI and suffer from slow inference.

To overcome these challenges, we introduce SlowFast-SCI, the first test-time adaptation-driven deep unfolding framework for efficient, self-adaptive spectral reconstruction. In the slow learning stage, we pre-train a deep unfolding backbone that fuses model-based priors with learnable parameters to acquire robust, general reconstruction capabilities. Furthermore, DUNs typically rely on numerous sequential stages to ensure high reconstruction fidelity, but this depth comes at the cost of heavy computation and slow inference. To address this, we apply an imaging mechanism-guided fast unfolding distillation step that compresses the pre-trained backbone into a streamlined “fast unfolding” variant with significantly reduced complexity. In the fast learning stage, lightweight Fast TTA modules (FAST-TTAMs) are inserted into each fast unfolding block

and self-supervisedly fine-tuned at test time, instantly aligning the model to new measurements while preserving the frozen backbone. By uniting offline robustness with on-the-fly adaptation, SlowFast-SCI achieves superior cross-domain generalization without additional labels.

With the backbone frozen, this design delivers swift test-time tuning and efficient inference, mirroring the human ability to rapidly leverage distilled knowledge for new experiences. We summarize our contributions as follows:

- We propose a unified dual-speed learning framework, SlowFast-SCI, which augments any deep unfolding network with offline pre-training for robust reconstruction and lightweight on-the-fly adaptation to new spectral configurations. To the best of our knowledge, this is the first test-time adaptation-driven, self-adaptive spectral unfolding framework.
- A imaging-guided fast unfolding distillation pipeline that compresses the pre-trained backbone into a fast unfolding variant, reducing parameter count and FLOPs by over 70% while preserving adaptability.
- We develop a lightweight self-supervised adaptation module embedded in each fast unfolding stage to enable rapid per-sample calibration at inference.
- Evaluation on standard Harvard, ICVL and real CASSI measurements, showing up to 5.79 dB PSNR gain on out-of-distribution (OOD) setups and a $4\times$ speedup in adaptation time.

2. Related Work

Hyperspectral Image Reconstruction. Related work comprises two main streams. Traditional optimization-based methods employ hand-crafted priors—such as sparsity [19, 36], total variation [31, 38], and low-rank constraints [20, 44]—to iteratively solve the inverse problem; while interpretable, they are limited by prior expressiveness and suffer from slow convergence. Deep learning and hybrid approaches accelerate SCI reconstruction [4–6, 12, 16, 42], including end-to-end networks, plug-and-play frameworks, and deep unfolding architectures (*e.g.*, DAUHST [6], RDLUF [12], DPU [42]). Although these learning-based methods deliver state-of-the-art accuracy and speed, they rely heavily on large paired datasets, making them brittle under optical variations or spectral distribution shifts at test time. In contrast, our work introduces a complementary paradigm: a self-supervised, test-time adaptation framework that enables rapid per-sample calibration without additional labeled data, thus improving robustness across unseen scenes.

Test-Time Adaptation. TTA adapts a pre-trained model during inference to improve performance without labeled test samples [11, 33]. In image reconstruction, TTA fine-tunes models at test time [27, 28, 47]. AdaptNet [47] integrates self-supervised test time training into deep unfolding networks, but its considerable depth leads to slow adapta-

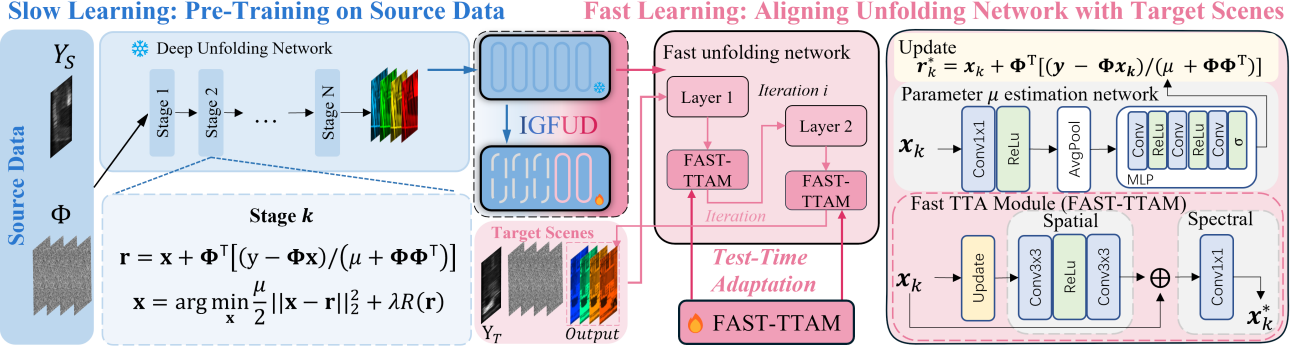


Figure 2. **Illustration of SlowFast-SCI.** The left side depicts the **slow learning** process, pre-training on the source data with a deep unfolding network. IGFUD distills the knowledge of the deep unfolding backbone into a compact fast unfolding network (FastUN). The right side shows the **fast learning** process, where FAST-TTAM rapidly adapts the FastUN to align the model with target scenes at inference time. The far right illustrates the details of FAST-TTAM, which takes both spatial and spectral information into account during fast learning. In contrast, we propose a lightweight adaptation module and a concise imaging-guided fast unfolding distillation pipeline, enabling efficient test-time adaptation via adapter architectures.

Model Distillation. Model distillation [3, 14] is a widely adopted method for transferring knowledge from a large teacher to a smaller student network. While initial methods used soft-label supervision, subsequent work extended distillation via intermediate feature matching [30] and attention transfer [40], and applied it to self-supervised learning [8] and TTA [37]. Existing distillation primarily targets semantic tasks, leaving inverse problems—especially SCI-based image reconstruction—largely unexplored. We address this by introducing a structural-knowledge distillation framework that transfers imaging priors from a pre-trained backbone into a lightweight, fast-unfolding student model. The student thus inherits the teacher’s robustness while remaining both efficient and adaptable during test-time.

3. Preliminaries

Mathematical Model of CASSI. SCI is a snapshot modality that captures a full hyperspectral data cube in a single coded measurement by jointly modulating and integrating across all spectral bands. Let a hyperspectral patch consist of N_λ bands $\{X_i\}_{i=1}^{N_\lambda}$, each $X_i \in \mathbb{R}^{H \times W}$. Each band is first modulated by a known binary mask M , then the modulated frames are shifted along the detector by $d(i-1)$ pixels and summed to yield the compressed measurement $Y(u, v) = \sum_{i=1}^{N_\lambda} M \odot X_i(u, v + d(i-1)) + N(u, v)$, where \odot denotes the Hadamard product, N is additive sensor noise, and (u, v) index spatial coordinates. By vectorizing the 3D hyperspectral cube into $x \in \mathbb{R}^{nN_\lambda}$ and the 2D measurement into $y \in \mathbb{R}^n$ with $n = H(W + d(N_\lambda - 1))$, the acquisition model can be written in matrix–vector form as:

$$y = \Phi x + n, \quad (1)$$

where $\Phi \in \mathbb{R}^{n \times nN_\lambda}$ encodes the combined masking and shifting operations. SCI reconstruction then consists of re-

covering the hyperspectral vector x from the single compressed measurement y given the known sensing matrix Φ .

In general, the deep unfolding networks formulate SCI reconstruction as a Bayesian problem, solving Eq. (1) under a unified MAP framework:

$$\hat{x}_{map} = \arg \min_x \log P(y|x) + \log P(x). \quad (2)$$

In particular, the original signal could be estimated by minimizing the following energy function:

$$\hat{x} = \arg \min_x \frac{1}{2} \|y - \Phi x\|_2^2 + \lambda R(x), \quad (3)$$

where $\frac{1}{2} \|y - \Phi x\|_2^2$ and $R(x)$ represent the data fidelity term and the image prior term respectively and λ is a trade-off hyperparameter. Among many solutions for Eq. (3), the HQS method can formulate the problem as an iterative scheme as follows:

$$r_{k+1} = x_k + \Phi^T [(y - \Phi x_k) / (\mu + \Phi \Phi^T)], \quad (4)$$

$$x_{k+1} = \arg \min_x \frac{\mu}{2} \|x - r_{k+1}\|_2^2 + \lambda R(x), \quad (5)$$

where μ is a penalty parameter. Based on the iterative scheme above, one can have a deep unfolding network with many stages. Within each stage, the x -sub problem can be regraded as a denoising problem, that is, to predict the original HSI signals x from their noisy counterparts $r = x + \epsilon$, which is solved by a learnable denoising network.

4. Method

SlowFast-SCI tackles two complementary challenges in SCI reconstruction with dual-speed learning. In the **slow learning** stage (Sec. 4.1), we overcome the ill-posed inverse problem and scarce HSI training data by pre-training a physics-guided unfolding backbone that fuses model priors with learnable parameters to learn robust, general reconstruction capabilities. In the **fast learning** stage (Sec. 4.2), we address domain shifts and per-sample variability by

inserting lightweight spectral adapters into each unfolding block and self-supervisedly fine-tuning only these adapters at test time—instantly calibrating to unseen measurements while keeping the backbone frozen. Furthermore, we propose an imaging-guided fast unfolding distillation framework that condenses the hybrid architecture into a compact “fast unfolding” network, augmented with tailored spectral adaptation blocks. This design enables efficient, label-free reconstruction across domains, mirroring the rapid application of distilled expertise in human learning.

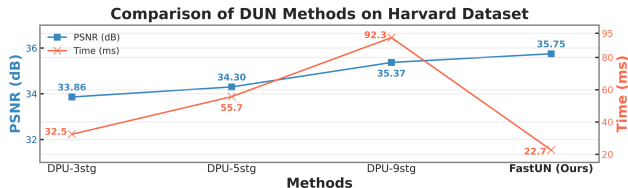


Figure 3. Comparison of DUN methods on 10 scenes of Harvard dataset. For all methods, PSNR (dB) and per-scene inference time (ms) are reported. For the unfolding method DPU, results with different numbers of stages are provided.

4.1. Slow Learning

In the slow learning stage, we pre-train a physics-guided unfolding backbone that integrates analytical priors with learnable parameters to address the ill-posed nature of spectral reconstruction and the scarcity of hyperspectral data. By explicitly embedding the underlying imaging physics into the network design, the unfolding backbone acquires a robust and generalizable reconstruction capability even under limited supervision.

Table 1. Comparison between the end-to-end (E2E) network and the deep unfolding network (DUN), both employing the same Transformer backbone.

Method	Category	PSNR(dB)
MST [5]	E2E	31.18
DAUHST [6]	DUN	32.64

As illustrated in Tab. 1, when employing the same backbone architecture (e.g., Transformer), the DUN generally achieves superior performance compared to its end-to-end counterpart. Furthermore, DUNs operate in a multi-stage iterative manner (e.g., 3, 5, or 9 stages), where increasing the number of stages progressively refines reconstruction performance at the cost of higher inference latency, as shown in Fig. 3. Building upon this foundation, the slow learning stage yields a 9-stage deep unfolding backbone with strong reconstruction accuracy. However, directly deploying this full-depth model in the fast learning stage is sub-optimal, as its considerable computational overhead limits efficiency and impedes rapid adaptation to novel scenes. To address these limitations, we propose Imaging-Guided Fast Unfolding Distillation (IGFUD), which bridges the gap between high-fidelity reconstruction and real-time adaptability by distilling the knowledge of the deep unfolding backbone into a compact fast unfolding network, thereby reducing model complexity while enabling unsupervised adaptation to unseen imaging conditions.

Imaging-Guided Fast Unfolding Distillation. The fast

Log-Scaled Visualization of $1/p$ -values for Different k -values

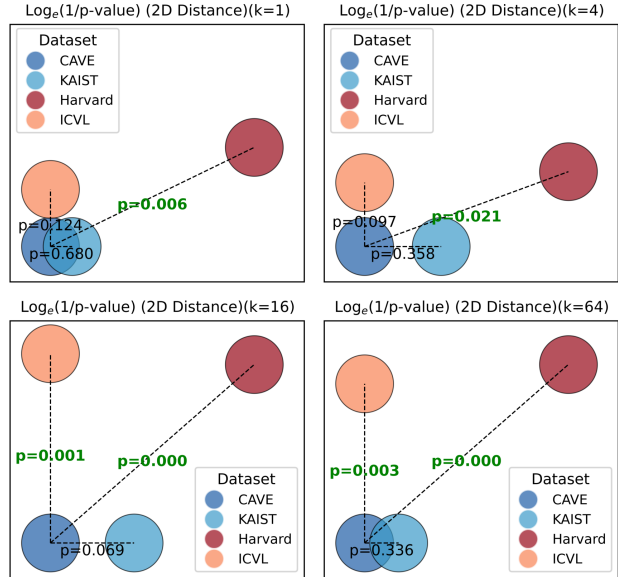


Figure 4. **Log-scaled visualization of $1/p$ -values for different k -values.** The p -values obtained by performing a permutation test ($n = 1000$) on the kernel matrices derived from the Maximum Mean Discrepancy (MMD) [29] between CAVE and the other three datasets (KAIST, Harvard, and ICVL). Each image (originally of size $256 \times 256 \times 28$) is processed using average pooling with different window sizes k . **Green bold** values indicate statistically significant differences ($p < 0.05$).

unfolding distillation (FUD) process is shown in Fig. 2. During this process, the pre-trained model, with its parameters frozen, serves as the slow unfolding network (SlowUN), while the two-stage model with the same architecture as the pre-trained model is used as fast unfolding network (FastUN). The dataset used for FUD is a dataset that the SlowUN has not seen during supervised slow learning, as shown in Fig. 5. Firstly, mask Φ and measurements $\{\mathbf{y}_i\}_{i=1}^{N_d} \in \mathbb{R}^{H \times (W+d \times (N_\lambda - 1))}$ are entered into the SlowUN to obtain the results $\{\mathbf{X}_{S,i}\}_{i=1}^{N_d} \in \mathbb{R}^{H \times W \times N_\lambda}$, which will be used as a label to supervise the training of FastUN. Then mask Φ and measurements $\{\mathbf{y}_i\}_{i=1}^{N_d}$ are input into FastUN to obtain the results $\{\mathbf{X}_{F,i}\}_{i=1}^{N_d}$. We update FastUN by minimizing the following loss:

$$\mathcal{L}_{FUD} = \frac{1}{N_d} \sum_{i=1}^{N_d} \|\mathbf{X}_{F,i} - \mathbf{X}_{S,i}\|_F^2. \quad (6)$$

The inference speed of the two-stage FastUN obtained by FUD is much faster than the original pre-trained model, and its performance on test data is comparable to that of the original pre-trained model, as shown in Fig. 3.

4.2. Fast Learning

Our slow-learning phase (Sec. 4.1) endows the deep unfolding network with robust physics-informed priors and learnable parameters (*i.e.*, the denoising network). However, when encountering a new spectral domain, naively fine-tuning all unfolding blocks requires nearly the same

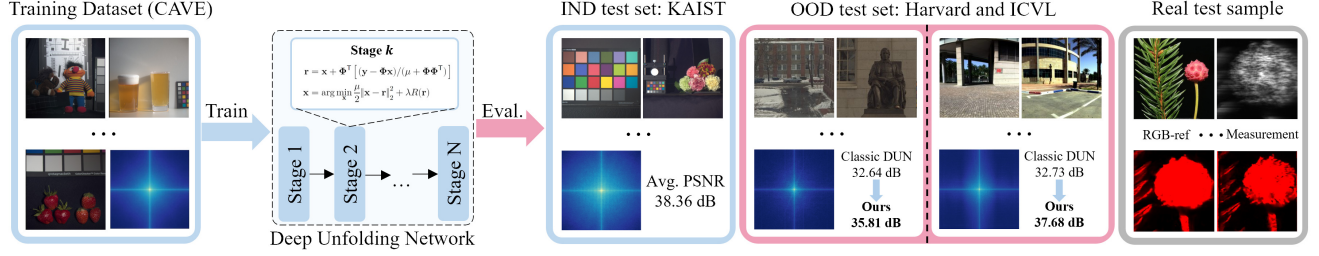


Figure 5. **Evaluating the cross-domain generalization of classic DUN.** Images with blue backgrounds represent the average log-spectrum of each dataset. The deep unfolding network is trained on the CAVE dataset during the slow learning stage. To evaluate cross-domain generalization, the model is tested on two out-of-distribution (OOD) datasets (Harvard and ICVL) and on real-world test samples, rather than on in-distribution (IND) datasets such as KAIST used in prior works. The average PSNR (dB) demonstrates that classic DUN performs well on IND test set but experiences a noticeable performance drop when applied to OOD test samples.

amount of data and computation as the original training process. Therefore, we aim to develop a more efficient strategy to adapt the model learned during the slow-learning stage.

Eqs. (4) and (5) formally describe the model obtained from the slow-learning phase, where Eq. (4) provides a closed-form solution that is independent of the data distribution. Accordingly, the component of the model that is highly sensitive to the data distribution resides in Eq. (5)—more precisely, in $R(\mathbf{r})$, which is modeled by a learnable denoising network during the slow-learning phase.

By roughly analyzing the statistical properties as a form of Bayesian inference of this denoising network, we design the Wiener-Filter-Inspired Adapter Modules, which enable the model to adapt efficiently to test samples whose distributions are similar to that of the training data. However, as illustrated in Figs. 4 and 5, the distributions of the two test datasets differ substantially from that of the training dataset. To bridge this distribution gap and further enhance the model’s adaptability, we propose Self-Adaptation-Driven Fast-Learning Unfolding.

4.2.1. Wiener-Filter-Inspired Adapter Modules

How to interpret the statistical properties of general CNNs within the framework of Bayesian inference remains an open question. For clarity of discussion, we denote the optimal denoising filter—*i.e.*, the Wiener filter—for each spectral channel λ_i corresponding to a training dataset \mathbf{x} and a specific test sample $\tilde{\mathbf{x}}$ as follows, respectively:

$$\hat{\mathcal{H}}_{w, \lambda_i}[k_1, k_2] = \frac{\mathbb{E}_{\mathbf{x}}\{|\hat{\mathbf{x}}_{\lambda_i}[k_1, k_2]|^2\}}{\mathbb{E}_{\mathbf{x}}\{|\hat{\mathbf{x}}_{\lambda_i}[k_1, k_2]|^2\} + \mathbb{E}_{\epsilon}\{|\hat{\epsilon}_{\lambda_i}[k_1, k_2]|^2\}}, \quad (7)$$

$$\hat{\mathcal{H}}_{w, \tilde{\mathbf{x}}, \lambda_i}[k_1, k_2] = \frac{|\hat{\tilde{\mathbf{x}}}_{\lambda_i}[k_1, k_2]|^2}{|\hat{\tilde{\mathbf{x}}}_{\lambda_i}[k_1, k_2]|^2 + \mathbb{E}_{\epsilon}\{|\hat{\epsilon}_{\lambda_i}[k_1, k_2]|^2\}}. \quad (8)$$

Here, $[k_1, k_2]$ denotes the spatial frequency components obtained via the discrete Fourier transform (DFT). For simplicity, inter-channel spectral correlations are neglected in this formulation. Detailed derivations of Eqs. (7) and (8) are provided in the supplementary material.

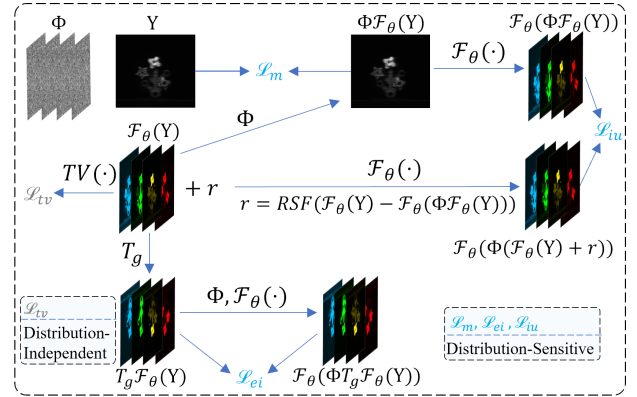


Figure 6. Illustration of four different self-supervised losses used in the fast learning stage. Φ , Y , and \mathcal{F}_θ denote the mask, measurement, and model, respectively. $TV(\cdot)$ represents the total variation loss, and RSF stands for random sign-flipping sampling. T_g denotes a set of geometric transformations (*e.g.*, shifts, rotations, *etc.*). The total variation loss \mathcal{L}_{tv} is distribution-independent, serving as a regularization term to preserve image smoothness, whereas \mathcal{L}_m , \mathcal{L}_{ei} , and \mathcal{L}_{iu} are distribution-sensitive.

4.2.2. Self-Adaptation-Driven Fast-Learning Unfolding

Adapter-Enhanced Unfolding Network Architecture.

Motivated by the analysis in Sec. 4.2.1, we propose an adapter-enhanced unfolding network (AdaptUN). AdaptUN is built upon our previously introduced FastUN (see Sec. 4.1) by appending a lightweight module—namely, the fast test-time adaptation module (FAST-TTAM)—after each unfolding stage. FAST-TTAM jointly leverages spatial and spectral cues to facilitate efficient test-time adaptation. During the adaptation phase, all parameters of the original unfolding backbone are frozen, and only the parameters within FAST-TTAM are learnable. The FAST-TTAM is a lightweight operator with one update step, one parameter μ estimation network, and two convolution blocks, the spatial convolution block and the spectral convolution block. The structure of parameter μ estimation network is shown in the upper right of Fig. 2, which is used to estimate the parameter μ . The spatial convolution block consists of two convolution layers with 3×3 filter and one ReLU function, while the spectral convolution block only includes one convolution layer with 1×1 filter.

Table 2. Comparisons (PSNR (upper entry in each cell), SSIM (lower entry in each cell), Params, and FLOPs) between SlowFast-SCI (SlowFast-SCI¹ and SlowFast-SCI² represent the slow-learning backbone we used were DAUHST and DPU, respectively.) and SOTA methods on 10 simulation scenes of Harvard dataset. Please see the supplementary materials for the complete comparison table.

Method	Reference	Params (M)	FLOPs (G)	S1	S2	S3	S4	S5	S6	S7	S8	S9	S10	Avg
TSA-Net [24]	ECCV 2020	42.20	91.58	30.54 0.795	25.76 0.557	30.27 0.750	22.24 0.422	36.71 0.845	27.62 0.820	27.51 0.610	24.83 0.644	27.23 0.570	22.79 0.490	27.55 0.650
RDLUF [12]	CVPR 2023	1.81	115.34	37.06 0.929	34.36 0.863	36.49 0.891	30.04 0.687	44.21 0.983	36.13 0.929	36.78 0.885	33.27 0.903	37.04 0.885	32.02 0.826	35.74 0.878
SSR-L [43]	CVPR 2024	5.18	78.93	36.25 0.921	33.60 0.838	35.38 0.880	29.01 0.666	43.23 0.978	36.41 0.924	35.79 0.863	33.57 0.890	35.87 0.860	30.03 0.745	34.91 0.857
DAUHST-SAH [41]	ECCV 2024	3.73	49.79	35.10 0.912	33.09 0.812	34.84 0.870	28.18 0.593	42.82 0.975	34.30 0.918	34.60 0.850	32.09 0.867	34.54 0.823	29.86 0.736	33.94 0.836
DPU-SAH [41]	ECCV 2024	3.12	54.44	36.93 0.932	34.41 0.853	36.04 0.884	30.19 0.697	43.43 0.980	35.51 0.930	36.20 0.867	33.61 0.895	36.80 0.874	31.02 0.779	35.41 0.869
DAUHST-9stg (slow learning) [6]	NeurIPS 2022	6.15	79.50	34.95 0.914	31.14 0.758	34.67 0.873	26.34 0.532	42.56 0.978	33.62 0.920	32.64 0.798	30.14 0.845	32.51 0.770	27.81 0.694	32.64 0.808
SlowFast-SCI¹	Ours	1.41	21.84	35.52 0.917	36.23 0.868	33.91 0.850	31.06 0.694	42.25 0.971	34.18 0.910	37.89 0.871	36.05 0.909	37.80 0.863	33.16 0.813	35.81 0.867
DPU-9stg (slow learning) [42]	CVPR 2024	2.85	49.26	36.90 0.932	34.36 0.852	36.02 0.884	30.14 0.695	43.41 0.980	35.45 0.930	36.14 0.866	33.56 0.894	36.72 0.873	30.97 0.777	35.37 0.868
SlowFast-SCI²	Ours	0.70	15.17	37.15 0.930	41.93 0.949	36.15 0.879	37.94 0.865	44.09 0.978	37.65 0.934	45.88 0.971	42.25 0.965	45.52 0.960	43.09 0.962	41.16 0.939

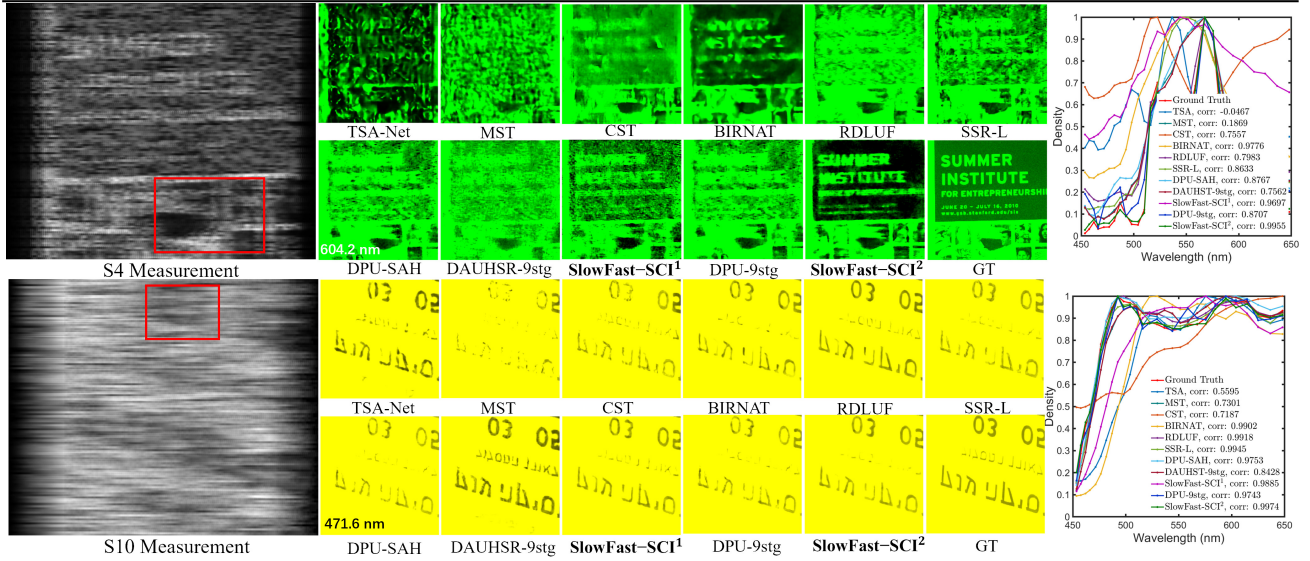


Figure 7. Simulated HSI reconstruction comparisons (middle) on Harvard (Scene 4) and ICVL (Scene 10). The left shows the scene measurement and the right shows the spectral curves corresponding to the selected region. Please zoom in for better view.

Self-Supervised Fine-tuning and Test-Time Adaptation. Consider AdaptUN: $\mathcal{F}_{AdaptUN}(\cdot; \omega^*, \theta)$:

$$\mathcal{F}_{AdaptUN}(\cdot; \omega^*, \theta) : \mathbf{y}, \Phi \rightarrow \mathbf{x}, \quad (9)$$

where ω^* denotes the parameters of FastUN frozen in self-supervised fine-tuning and test-time adaptation and θ denotes the parameters of the adapt layers to be updated. Given the same dataset $\{\mathbf{y}_i\}_{i=1}^{N_d}$ as in IGFUD, we update θ by minimizing the following self-supervised loss:

$$\mathcal{L}_{sst} = \mathcal{L}_m + \omega_1 \mathcal{L}_{ei} + \omega_2 \mathcal{L}_{iu} + \omega_3 \mathcal{L}_{tv}. \quad (10)$$

This self-supervised loss is motivated by [41], where \mathcal{L}_m , \mathcal{L}_{ei} , \mathcal{L}_{iu} , and \mathcal{L}_{tv} denote the measurement consistency loss, equivariance imaging loss, image uncertainty loss, and total variation loss, respectively, as illustrated in Fig. 6. The coefficients ω_1 , ω_2 , and ω_3 represent the equilibrium constants. Please refer to the supplementary material for more details. Let $\hat{\theta}$ denote the parameters of the adapt layers after self-supervised fine-tuning. Then, given a test sample $\tilde{\mathbf{y}}$ that is not in $\{\mathbf{y}_i\}_{i=1}^{N_d}$, we adapt model $\mathcal{F}_{AdaptUN}(\cdot; \omega^*, \hat{\theta})$ to $\tilde{\mathbf{y}}$ by minimizing self-supervised loss \mathcal{L}_{tta} :

$$\mathcal{L}_{tta} = \mathcal{L}_m + \alpha \mathcal{L}_{ei}, \quad (11)$$

Table 3. Comparisons (PSNR (upper entry in each cell), SSIM (lower entry in each cell), Params, and FLOPs) between SlowFast-SCI and SOTA methods on 10 simulation scenes of ICVL dataset. Please see the supplementary materials for the complete comparison table.

Method	Reference	Params (M)	FLOPs (G)	S1	S2	S3	S4	S5	S6	S7	S8	S9	S10	Avg
TSA-Net [24]	ECCV 2020	42.20	91.58	26.22 0.720	28.50 0.736	28.02 0.777	26.32 0.819	31.10 0.736	28.23 0.750	20.91 0.783	25.14 0.762	28.74 0.700	27.25 0.817	27.05 0.760
RDLUF [12]	CVPR 2023	1.81	115.34	36.67 0.953	41.16 0.970	40.79 0.975	40.93 0.971	45.72 0.983	39.34 0.959	34.12 0.956	34.73 0.928	39.87 0.951	37.27 0.960	39.06 0.961
SSR-L [43]	CVPR 2024	5.18	78.93	35.77 0.938	41.14 0.968	39.39 0.966	41.20 0.970	45.53 0.982	39.69 0.960	33.24 0.947	34.72 0.922	38.90 0.942	37.30 0.946	38.69 0.954
DAUHST-SAH [41]	ECCV 2024	3.73	49.79	29.94 0.902	34.24 0.937	34.50 0.936	32.88 0.934	39.74 0.962	34.98 0.929	26.37 0.893	29.82 0.879	37.23 0.926	28.39 0.878	32.81 0.918
DPU-SAH [41]	ECCV 2024	3.12	54.44	33.90 0.940	39.55 0.966	38.12 0.971	39.82 0.967	45.26 0.981	39.36 0.960	28.31 0.919	32.63 0.918	39.76 0.951	35.85 0.950	37.26 0.952
DAUHST-9stg (slow learning) [6]	NeurIPS 2022	6.15	79.50	29.49 0.902	34.26 0.941	34.43 0.938	32.83 0.938	39.94 0.966	35.07 0.932	25.59 0.890	29.61 0.883	37.45 0.932	28.59 0.883	32.73 0.920
SlowFast-SCI¹	Ours	1.41	21.84	35.48 0.936	39.99 0.964	38.91 0.963	39.73 0.964	43.86 0.975	37.55 0.946	32.23 0.938	34.31 0.921	38.40 0.934	36.35 0.952	37.68 0.950
DPU-9stg (slow learning) [42]	CVPR 2024	2.85	49.26	33.88 0.939	39.51 0.966	38.09 0.971	39.76 0.966	45.21 0.981	39.32 0.960	28.29 0.919	32.61 0.918	39.74 0.951	35.81 0.950	37.22 0.952
SlowFast-SCI²	Ours	0.70	15.17	38.59 0.962	41.33 0.970	41.54 0.979	42.15 0.972	45.49 0.981	39.22 0.957	35.72 0.957	36.16 0.937	39.45 0.949	38.26 0.962	39.79 0.963

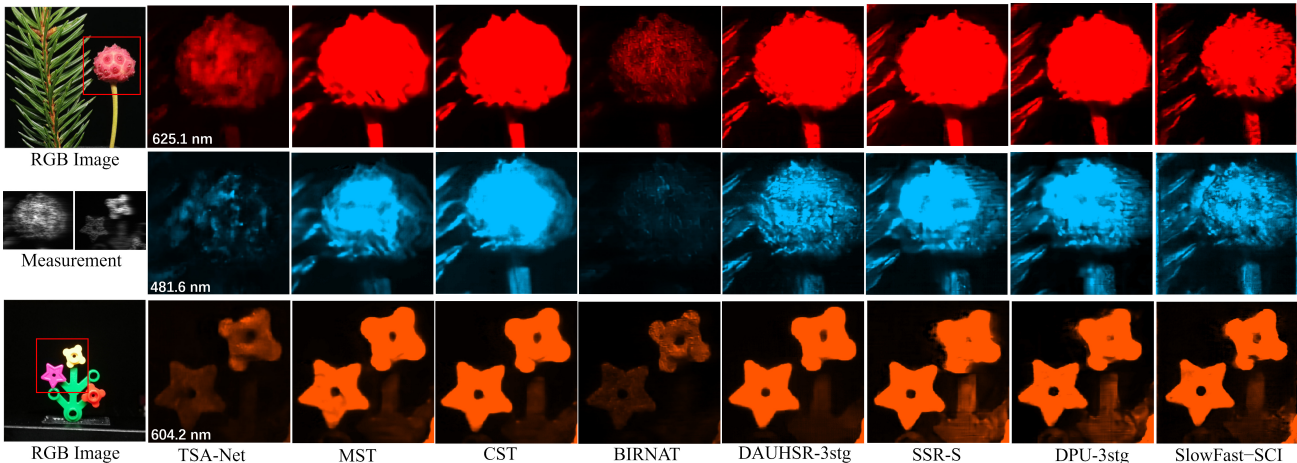


Figure 8. Real-scene HSI reconstruction results. Shown are reconstructions of two real-world scenes across selected spectral channels (out of 28), using various state-of-the-art methods. Compared to others, SlowFast-SCI restores finer details and better suppresses noise, highlighting its effectiveness in real-data scenarios.

where α denote the equilibrium constant. To balance efficiency and feasibility, only the two most critical components of the aforementioned self-supervised losses—the measurement consistency loss and the equivariance imaging loss—are utilized during the test time adaptation stage.

5. Experiments

5.1. Experiment Setup

Datasets. The pre-trained model used in slow learning was trained on the CAVE [26] dataset. We adopted two datasets Harvard [9] and ICVL [1] with randomly clipped patches of size $256 \times 256 \times 28$ for simulation experiments.

Comparison Methods. We compare our SlowFast-SCI on synthetic data and real scenes with state-of-the-art

(SOTA) reconstruction methods including TSA-Net [24], MST[5], CST[4], BIRNAT[7], RDLUF[12], SSR-L [43], SAH-SCI [41], DAUHST [6], and DPU [42].

Implementation Details. The implementation details of SlowFast-SCI are given in the supplementary materials.

5.2. Quantitative Results

Comparison on Harvard and ICVL. Tab. 2 and 3 summarize PSNR, SSIM, Params, and FLOPs for SlowFast-SCI¹ (slow-learning backbone: DAUHST) and SlowFast-SCI² (slow-learning backbone: DPU) against SOTA methods. SlowFast-SCI² achieves 41.16dB/0.939 on Harvard and 39.79dB/0.963 on ICVL, outperforming all competitors. SlowFast-SCI¹ yields 35.81dB/0.867 and 37.68dB/0.950, improving its backbone by 9.71%/7.30%

on Harvard and 15.12%/3.26% on ICVL. Both variants use <25% of the Params and <33% of the FLOPs of their backbones. Compared to SAH-SCI, SlowFast-SCI² achieves 16.24%/8.06% and 6.79%/1.16% gains on Harvard and ICVL, respectively, with lower resource costs; SlowFast-SCI¹ attains similar improvements.

5.3. Qualitative Results

Simulation Data Results. Fig. 7 depicts the simulation HSI reconstruction comparisons between our method and other SOTA methods on Harvard and ICVL datasets, respectively. It can be seen that the other models produce poor reconstruction results with a lot of noise and artifacts, since they lack fast learning on similar data. The results of our SlowFast-SCI in different bands show that the proposed dual speed framework can correct the problem of weak generalization ability of SCI reconstruction due to insufficient training data. This is because our method enhances the generalization of the model to extract more spectral information through self-supervised fast learning and can adapt the model to align it with target scenes at inference. Besides, the spectral density curves show that the reconstruction results of SlowFast-SCI are more similar and correlated with the GT, which proves our method is capable of improving the spectral-dimension consistency of the model.

Real-Scene HSI Reconstruction. We evaluate SlowFast-SCI on real-world HSI using CAVE and KAIST [10], pre-training a two-stage DPU backbone with real CASSI masks under the protocols of Zhang et al. [42], Meng et al. [24], and Cai et al. [6]. To simulate realistic noise, we inject 11-bit shot noise during both slow- and fast-learning. At test time, raw measurements serve as self-supervised labels for adaptation. As shown in Fig. 8, SlowFast-SCI recovers finer details and suppresses noise more effectively than SOTAs, demonstrating strong real-world potential. We also provide additional visual comparisons of SlowFast-SCI against SOTAs on scenes from the Harvard, ICVL datasets and real dataset—see the Supplementary Material for details.

Table 4. Ablation on the stages of fast unfolding network, FAST-TTAM, and Test-time adaptation.

Case	Stages	FAST-TTAM	TTA	PSNR	SSIM	Params (M)	FLOPs (G)	Time (s)
(a)	9	×	×	35.37	0.868	2.85	49.26	—
(b)	9	✓	×	34.93	0.850	3.16	67.92	—
(c)	9	✓	✓	33.75	0.825	3.16	67.92	~45.9
(d)	1	×	×	35.67	0.876	0.32	5.39	—
(e)	1	✓	×	38.39	0.912	0.35	7.63	—
(f)	1	✓	✓	38.39	0.903	0.35	7.63	—
(g)	2	×	×	35.75	0.876	0.64	10.86	—
(h)	2	✓	×	39.97	0.932	0.70	15.17	—
(i)	2	✓	✓	41.16	0.939	0.70	15.17	~10.9

5.4. Ablation Studies

Fast Unfolding-Stage Configuration Analysis. We assess the effect of different unfolding stages on performance using the Harvard dataset (Tab. 4), where FAST-TTAM denotes the unfolding layer is attached by the adaptation mod-

ule. Using the 9-stage DPU as a baseline (case a), results from cases (a, d, g) show that both 1-stage and 2-stage variants preserve the key characteristics of the original model. However, cases (e, h) and (f, i) show that the 1-stage variant learns less effectively than the 2-stage network. Thus, despite its faster inference, the 1-stage model is discarded in favor of the better-performing 2-stage variant that enables a balance between reconstruction quality and inference speed. In particular, case (c) can be regarded as the implementation of AdaptNet [46] under the SCI configuration. Notably, AdaptNet fails to adapt to OOD data and suffers from slow inference. In contrast, case (i) demonstrates that our proposed method not only achieves effective test-time alignment with OOD test samples but also significantly accelerates inference.

Fast Learning Ablation. We analyze the performance of FAST-TTAM and TTA in the fast learning. Tab. 4 (d, e) and (g, h) show that the proposed FAST-TTAM can effectively transfer the fast unfolding variant to the target domain through self-supervised fine-tuning. Besides, case (h, i) in Tab. 4 shows self-supervised test-time adaptation can further align the fast unfolding variant with target scenes.

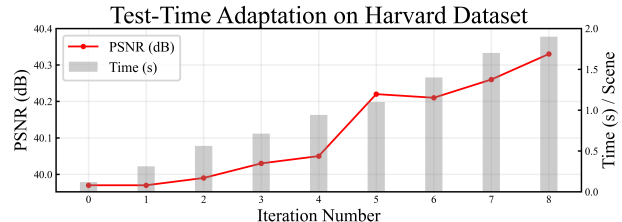


Figure 9. Ablation on iteration times at inference.

Iteration Times at Inference. This experiment shows the relationship between iteration times and performance gains through TTA. Fig. 9 shows that as the number of iterations increases, the PSNR improves, and the required inference time also increases accordingly. Only a few iterations are needed to achieve impressive performance, which proves the effectiveness of our method.

6. Conclusion

We have introduced SlowFast-SCI, to the best of our knowledge the first test-time adaptation-driven, self-adaptive spectral unfolding framework. By adopting a dual-speed paradigm—distilling a priors-driven backbone into a compact “fast unfolding” network during offline training, then embedding lightweight, self-supervised adapters for on-the-fly calibration—our method achieves over 70% parameter and FLOPs reduction, up to 5.79 dB PSNR improvement on out-of-distribution data, and a 4× faster adaptation runtime, all while preserving robust cross-domain performance.

Crucially, SlowFast-SCI’s modularity allows it to be seamlessly integrated into any deep unfolding architecture, unlocking real-time hyperspectral reconstruction on resource-constrained platforms—ranging from aerial

drones, point-of-care scanners to distributed environmental sensors. We believe this work paves the way for a new class of self-adaptive, field-deployable imaging systems and look forward to exploring extensions to other computational imaging modalities and richer adaptation objectives.

Limitation and Future Work: Despite their small footprint, SlowFast-SCI’s per-sample adapters introduce minor latency, posing challenges for ultra-low-power or real-time deployment. Our study focuses on disperser-based CASSI; future work will extend the dual-speed paradigm to other SCI forms and unfolding models, with emphasis on hardware-efficient adapters, early-exit schemes, and broader imaging applications.

References

- [1] Boaz Arad and Ohad Ben-Shahar. Sparse recovery of hyper-spectral signal from natural rgb images. In *Computer Vision–ECCV 2016: 14th European Conference, Amsterdam, the Netherlands, October 11–14, 2016, Proceedings, Part VII 14*, pages 19–34. Springer, 2016. 7
- [2] Marcus Borengasser, William S Hungate, and Russell Watkins. *Hyperspectral remote sensing: principles and applications*. CRC press, 2007. 2
- [3] Cristian Buciluă, Rich Caruana, and Alexandru Niculescu-Mizil. Model compression. In *Proceedings of the 12th ACM SIGKDD international conference on Knowledge discovery and data mining*, pages 535–541, 2006. 3
- [4] Yuanhao Cai, Jing Lin, Xiaowan Hu, Haoqian Wang, Xin Yuan, Yulun Zhang, Radu Timofte, and Luc Van Gool. Coarse-to-fine sparse transformer for hyperspectral image reconstruction. In *ECCV*, 2022. 2, 7
- [5] Yuanhao Cai, Jing Lin, Xiaowan Hu, Haoqian Wang, Xin Yuan, Yulun Zhang, Radu Timofte, and Luc Van Gool. Mask-guided spectral-wise transformer for efficient hyperspectral image reconstruction. In *CVPR*, 2022. 4, 7
- [6] Yuanhao Cai, Jing Lin, Haoqian Wang, Xin Yuan, Henghui Ding, Yulun Zhang, Radu Timofte, and Luc Van Gool. Degradation-aware unfolding half-shuffle transformer for spectral compressive imaging. In *NeurIPS*, 2022. 2, 4, 6, 7, 8
- [7] Yuanhao Cai, Yuxin Zheng, Jing Lin, Xin Yuan, Yulun Zhang, and Haoqian Wang. Binarized spectral compressive imaging. In *NeurIPS*, 2023. 2, 7
- [8] Mathilde Caron, Hugo Touvron, Ishan Misra, Hervé Jégou, Julien Mairal, Piotr Bojanowski, and Armand Joulin. Emerging properties in self-supervised vision transformers. In *Proceedings of the IEEE/CVF international conference on computer vision*, pages 9650–9660, 2021. 3
- [9] Ayan Chakrabarti and Todd Zickler. Statistics of real-world hyperspectral images. In *CVPR 2011*, pages 193–200. IEEE, 2011. 7
- [10] Inchang Choi, MH Kim, D Gutierrez, DS Jeon, and G Nam. High-quality hyperspectral reconstruction using a spectral prior. Technical report, 2017. 8
- [11] Mohammad Zalbagi Darestani, Jiayu Liu, and Reinhard Heckel. Test-time training can close the natural distribution shift performance gap in deep learning based compressed sensing. In *International conference on machine learning*, pages 4754–4776. PMLR, 2022. 2
- [12] Yubo Dong, Dahua Gao, Tian Qiu, Yuyan Li, Minxi Yang, and Guangming Shi. Residual degradation learning unfolding framework with mixing priors across spectral and spatial for compressive spectral imaging. In *Proceedings of the IEEE/CVF Conference on Computer Vision and Pattern Recognition (CVPR)*, pages 22262–22271, 2023. 2, 6, 7
- [13] Michael E Gehm, Renu John, David J Brady, Rebecca M Willett, and Timothy J Schulz. Single-shot compressive spectral imaging with a dual-disperser architecture. *Optics express*, 15(21):14013–14027, 2007. 1
- [14] Geoffrey Hinton, Oriol Vinyals, and Jeff Dean. Distilling the knowledge in a neural network. *arXiv preprint arXiv:1503.02531*, 2015. 3
- [15] Yining Hong, Beide Liu, Maxine Wu, Yuanhao Zhai, Kai-Wei Chang, Linjie Li, Kevin Lin, Chung-Ching Lin, Jianfeng Wang, Zhengyuan Yang, et al. Slowfast-vgen: Slowfast learning for action-driven long video generation. *arXiv preprint arXiv:2410.23277*, 2024. 1
- [16] Xiaowan Hu, Yuanhao Cai, Jing Lin, Haoqian Wang, Xin Yuan, Yulun Zhang, Radu Timofte, and Luc Van Gool. Hd-net: High-resolution dual-domain learning for spectral compressive imaging. In *CVPR*, 2022. 2
- [17] Tao Huang, Weisheng Dong, Xin Yuan, Jinjian Wu, and Guangming Shi. Deep gaussian scale mixture prior for spectral compressive imaging. In *Proceedings of the IEEE/CVF Conference on Computer Vision and Pattern Recognition*, pages 16216–16225, 2021. 2
- [18] Min H Kim, Todd Alan Harvey, David S Kittle, Holly Rushmeier, Julie Dorsey, Richard O Prum, and David J Brady. 3d imaging spectroscopy for measuring hyperspectral patterns on solid objects. *ACM Transactions on Graphics (TOG)*, 31(4):1–11, 2012. 1
- [19] David Kittle, Kerkil Choi, Ashwin Wagadarikar, and David J Brady. Multiframe image estimation for coded aperture snapshot spectral imagers. *Applied optics*, 49(36):6824–6833, 2010. 2
- [20] Yang Liu, Xin Yuan, Jinli Suo, David J Brady, and Qionghai Dai. Rank minimization for snapshot compressive imaging. *IEEE transactions on pattern analysis and machine intelligence*, 41(12):2990–3006, 2018. 2
- [21] Guolan Lu and Baowei Fei. Medical hyperspectral imaging: a review. *Journal of biomedical optics*, 19(1):010901–010901, 2014. 1
- [22] James L McClelland, Bruce L McNaughton, and Randall C O’Reilly. Why there are complementary learning systems in the hippocampus and neocortex: insights from the successes and failures of connectionist models of learning and memory. *Psychological review*, 102(3):419, 1995. 1
- [23] Ziyi Meng, Shirin Jalali, and Xin Yuan. Gap-net for snapshot compressive imaging. *arXiv preprint arXiv:2012.08364*, 2020. 2
- [24] Ziyi Meng, Jiawei Ma, and Xin Yuan. End-to-end low cost compressive spectral imaging with spatial-spectral self-attention. In *European conference on computer vision*, pages 187–204. Springer, 2020. 1, 2, 6, 7, 8

- [25] Ziyi Meng, Mu Qiao, Jiawei Ma, Zhenming Yu, Kun Xu, and Xin Yuan. Snapshot multispectral endomicroscopy. *Opt. Lett.*, 45(14):3897–3900, 2020. 2
- [26] Jong-II Park, Moon-Hyun Lee, Michael D Grossberg, and Shree K Nayar. Multispectral imaging using multiplexed illumination. In *2007 IEEE 11th International Conference on Computer Vision*, pages 1–8. IEEE, 2007. 7
- [27] Xinran Qin, Yuhui Quan, Tongyao Pang, and Hui Ji. Ground-truth free meta-learning for deep compressive sampling. In *Proceedings of the IEEE/CVF Conference on Computer Vision and Pattern Recognition (CVPR)*, pages 9947–9956, 2023. 2
- [28] Yuhui Quan, Xinran Qin, Tongyao Pang, and Hui Ji. Dual-domain self-supervised learning and model adaption for deep compressive imaging. In *Computer Vision—ECCV 2022: 17th European Conference, Tel Aviv, Israel, October 23–27, 2022, Proceedings, Part XXX*, pages 409–426, 2022. 2
- [29] Stephan Rabanser, Stephan Günnemann, and Zachary Lipton. Failing loudly: An empirical study of methods for detecting dataset shift. *Advances in Neural Information Processing Systems*, 32, 2019. 4
- [30] Adriana Romero, Nicolas Ballas, Samira Ebrahimi Kahou, Antoine Chassang, Carlo Gatta, and Yoshua Bengio. Fitnets: Hints for thin deep nets. *arXiv preprint arXiv:1412.6550*, 2014. 3
- [31] Leonid I Rudin, Stanley Osher, and Emad Fatemi. Nonlinear total variation based noise removal algorithms. *Physica D: nonlinear phenomena*, 60(1-4):259–268, 1992. 2
- [32] Gladys C Schwesinger. Review of “psychological development” by norman l. munn. *Pedagogical Seminary and Journal of Genetic Psychology*, 55, 1955. 1
- [33] Yu Sun, Xiaolong Wang, Zhuang Liu, John Miller, Alexei Efros, and Moritz Hardt. Test-time training with self-supervision for generalization under distribution shifts. In *International conference on machine learning*, pages 9229–9248. PMLR, 2020. 2
- [34] Endel Tulving. Elements of episodic memory. *Oxford University Press*, 1983. 1
- [35] Hien Van Nguyen, Amit Banerjee, and Rama Chellappa. Tracking via object reflectance using a hyperspectral video camera. In *2010 IEEE Computer Society Conference on Computer Vision and Pattern Recognition-Workshops*, pages 44–51. IEEE, 2010. 1
- [36] Ashwin Wagadarikar, Renu John, Rebecca Willett, and David Brady. Single disperser design for coded aperture snapshot spectral imaging. *Applied optics*, 47(10):B44–B51, 2008. 1, 2
- [37] Dequan Wang, Evan Shelhamer, Shaoteng Liu, Bruno Olshausen, and Trevor Darrell. Tent: Fully test-time adaptation by entropy minimization. In *International Conference on Learning Representations*, 2021. 3
- [38] Lizhi Wang, Zhiwei Xiong, Dahua Gao, Guangming Shi, and Feng Wu. Dual-camera design for coded aperture snapshot spectral imaging. *Applied optics*, 54(4):848–858, 2015. 2
- [39] Yuan Yuan, Xiangtao Zheng, and Xiaoqiang Lu. Hyperspectral image superresolution by transfer learning. *IEEE Journal of Selected Topics in Applied Earth Observations and Remote Sensing*, 10(5):1963–1974, 2017. 2
- [40] Sergey Zagoruyko and Nikos Komodakis. Paying more attention to attention: Improving the performance of convolutional neural networks via attention transfer. In *ICLR*, 2017. 3
- [41] Haijin Zeng, Yuxi Liu, Yongyong Chen, Youfa Liu, Chong Peng, and Jingyong Su. Sah-sci: Self-supervised adapter for efficient hyperspectral snapshot compressive imaging. In *ECCV*, 2024. 2, 6, 7
- [42] Jiancheng Zhang, Haijin Zeng, Jiezhong Cao, Yongyong Chen, Dengxiu Yu, and Yin-Ping Zhao. Dual prior unfolding for snapshot compressive imaging. In *Proceedings of the IEEE/CVF Conference on Computer Vision and Pattern Recognition (CVPR)*, pages 25742–25752, 2024. 2, 6, 7, 8
- [43] Jiancheng Zhang, Haijin Zeng, Yongyong Chen, Dengxiu Yu, and Yin-Ping Zhao. Improving spectral snapshot reconstruction with spectral-spatial rectification. In *Proceedings of the IEEE/CVF Conference on Computer Vision and Pattern Recognition (CVPR)*, pages 25817–25826, 2024. 2, 6, 7
- [44] Shipeng Zhang, Lizhi Wang, Ying Fu, Xiaoming Zhong, and Hua Huang. Computational hyperspectral imaging based on dimension-discriminative low-rank tensor recovery. In *Proceedings of the IEEE/CVF International Conference on Computer Vision*, pages 10183–10192, 2019. 2
- [45] Xuanyu Zhang, Yongbing Zhang, Ruiqin Xiong, Qilin Sun, and Jian Zhang. Herosnet: Hyperspectral explicable reconstruction and optimal sampling deep network for snapshot compressive imaging. In *Proceedings of the IEEE/CVF Conference on Computer Vision and Pattern Recognition*, pages 17532–17541, 2022. 1
- [46] Yutian Zhao, Tianjing Zhang, and Hui Ji. Test-time model adaptation for image reconstruction using self-supervised adaptive layers. In *ECCV*, 2024. 8
- [47] Yutian Zhao, Tianjing Zhang, and Hui Ji. Test-time model adaptation for image reconstruction using self-supervised adaptive layers. In *ECCV*, 2024. 2